Research Article

High-pressure study of the aurophilic topological Dirac material AuI

Jaspreet Singh[a], Sushree Sarita Sahoo[a], Kanchana Venkatakrishnan[a,*],
Ganapathy Vaitheeswaran[b,*], Daniel Errandonea[c,*]

[a] Department of Physics, Indian Institute of Technology Hyderabad, Kandi, 502 285 Sangareddy, Telangana, India
[b] School of Physics, University of Hyderabad, Prof. C. R. Rao Road, Gachibowli, Hyderabad 500 046, Telangana, India
[c] Departamento de Fisica Aplicada-ICMUV-MALTA Consolider Team, Universidad de Valencia, C/Dr. Moliner 50, 46100 Burjassot, Valencia, Spain

ARTICLE INFO

ABSTRACT

We endeavour to explore the high-pressure study in the aurophilic AuI within the state-of-the-art of first principles. The impediment of expressing precise ground-state features of aurophilic compounds that had afflicted prior theoretical research has been resolved by incorporating van der Waals corrections (vdw). Mechanical and dynamical stability are ensured at ambient using the computed elastic constants and phonon dispersion curves. The dynamical instability is triggered by the application of pressure in AuI, as evidenced by the softening of an acoustic mode (E_u) at ~7 GPa. Non-adherence of estimated elastic constants to the Born stability criterion at this pressure illustrates the system's mechanical instability. As previously demonstrated in experiments, the pressure-driven amorphization is rationalised by the phonon softening and elastic instability. Our calculations of the electronic band structure reveal an indirect bandgap (2.31 eV). Z_2 invariants confirm that non-symmorphic AuI is a non-trivial Dirac material with the inclusion of spin-orbit coupling. Furthermore, a type-A hourglass dispersion with movable Dirac point is observed at the two-fold screw rotation axis (C_{2y}). The pressure-dependent electronic structure reveal that the band topology is unaffected by pressure up to amorphous state. Our findings predict that this aurophilic class of material AuI possess exotic structural and electronic properties, encouraging further studies.

© 2022 The Author(s). Published by Elsevier B.V. This is an open access article under the CC BY-NC-ND license (http://creativecommons.org/licenses/by-nc-nd/4.0/).

1. Introduction

In recent years, studying the behaviour of matter under extreme pressure conditions has become an intriguing and challenging research topic. Using high-pressure (HP) techniques, new materials with specifically designed properties can be produced in crystalline and amorphous states [1]. Pressure-induced amorphization (PIA) is a first-order transition between crystalline and amorphous phases that dramatically changes the structure of the solid [2]. This phenomenon has been observed in different compounds for the past few years. PIA occurs in a range of compounds with various bonding types, including covalent (SiO_2), ionic ($LiKSO_4$), molecular (SnI_4), and hydrogen bonding (H_2O) [3–6]. Likewise, amorphization at HP is also found in more complex bonded systems such as silicates [7], tungstates [8], molybdates [9], and other minerals [10]. Many variables have been linked to PIA, including poly-tetrahedral packing [11], an increase in the coordination number [12], and polyatomic ion orientational disorder [13]. The PIA was first conceived in response to

kinetic impediment in equilibrium phase transitions [14]. However, alternatively, an elastic instability can also drive amorphization [15].

Recently, a pressure-induced irreversible amorphization has been reported at 10.7 GPa in gold iodide (AuI) [16]. This compound consists of polymeric *Au−I* zigzag chains linked via *Au···Au* aurophilic interactions forming two-dimensional (2D) layers, which are held together by weak van der Waals forces among *I* atoms. Amorphization was not anticipated in such a layered compound. Instead, a transition to a higher symmetry structure (typically cubic) was expected because of its anisotropic response to pressure due to the existence of directional weak van der Waals bonds [17]. Under HP, a cubic structure similar to AgI and CuI would be expected in AuI if it behaved like other 2D-layered binary compounds [18]. There is currently no theoretical explanation for the observed pressure-driven amorphization. This is owing to the difficulties that density-functional theory (DFT) has in effectively describing aurophilic substances [19]. Previous DFT simulations of AuI at ambient pressure were inadequate in generating a suitable crystal structure [20,21]. This feature prompted us to conduct a DFT investigation of AuI to learn more about its characteristics and its behaviour under compression. Another interesting and unexplored fact about AuI is related to the spin-orbit coupling (SOC) associated with gold. In

tetragonal crystals with a significant SOC, symmetry-enforced topological band crossings should exist, which might be Dirac or Weyl points [22]. Exotic surface states [23], unique magneto transport [24], inherent anomalous Hall effect [25], high thermopower [26], and exotic phenomena connected to quantum anomalies [27] are all examples of topological band crossings. The examination of the system's symmetry and topological invariants that depend on translational symmetry are used in standard theoretical approaches for the search and categorisation of topological features in materials [28,29]. Interestingly, AuBr, which is isomorphic to AuI, possesses movable Dirac points that form hourglass dispersions and exhibit a non-trivial topology defined by a Z_2 invariant, that is imposed by band connectivity [22]. It is, therefore, interesting to study the topology of the band structure of AuI, at ambient- and high-pressure, to search for possible band crossings.

Using state-of-the-art van der Waals corrected DFT, we investigated the physical properties of AuI and the impact of pressure on them. Structural, elastic, and vibrational features have been emphasised to explain the known pressure-driven amorphization [16]. We also estimated electronic band structure of AuI and observed that it is a three-dimensional Dirac material with movable Dirac points together with hourglass dispersion up to the amorphization pressure.

2. Computational details

The geometry was optimised using the Projector-Augmented Wave (PAW) method, which was employed in VASP in the framework of density-functional theory (DFT) [30]. The Perdew-Burke-Ernzerhof (PBE) potentials within the Generalized-Gradient Approximation (GGA) were used for the exchange-correlation functionals [31]. For all computations, the plane wave energy cut-off was set to 520 eV. A value of 10^{-6} eV has been used as the energy convergence criterion. A 14 × 14 × 4 k-mesh has been implemented for geometry optimisation computations according to the Monkhorst-Pack technique [32]. Van der Waals contributions have been included to account for the interaction of the gold-iodine layers in AuI. Grimme D2 method (IVDW = 1) [33], Grimme D3 method with zero damping (IVDW = 11) [34], and D3 method with Becke-Jonson damping (IVDW = 12) [35] were used to calculate van der Waals corrections. Phonon-dispersion calculations have been performed using the density-functional perturbation theory with VASP and Phonopy [36]. Fitting the pressure-volume (P-V) data to a third-order Birch-Murnaghan equation of state (EOS) [37] yielded the bulk modulus and its pressure derivative for AuI. Both with and without SOC, the electronic structure computations have been performed. For SOC calculations, the first-principles results were fitted to a tight-binding Hamiltonian using maximally localised Wannier functions (MLWF) [38]. The topological characteristics of the compound based on the tight-binding model were studied using the iterative Green's function technique, which is implemented in the WANNIERTOOLS package [39,40].

3. Results and discussion

3.1. Structural properties

AuI crystallises in a polymeric tetragonal structure with space group $P4_2/ncm$ (No. 138). Fig. 1 depicts the crystal structure. In its traditional unit cell, this structure has four formula units. The Perdew-Burke-Ernzerhof (PBE) functional [31] has been used to get the ground state of AuI. Different van der Waals corrections (IVDW1 [33], IVDW11 [34], IVDW12 [35], etc.) schemes, were also used to obtain the optimised parameters. Our calculations succeeded in modelling the crystal structure of AuI, in contrast to prior DFT investigations [20,21], which did not predict the tetragonal structure
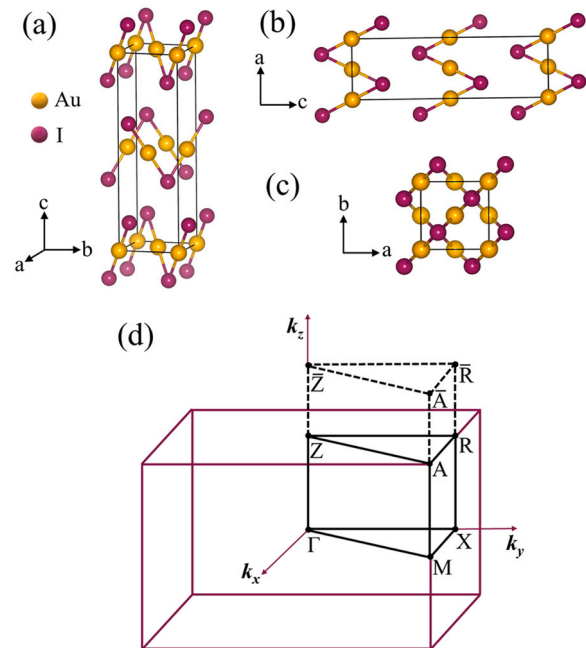

Fig. 1. (a–c) Crystal structure of AuI viewed along different projections, and (d) high-symmetry points in the irreducible Brillouin zone (BZ) and the BZ projection plane onto the (001) direction.

Table 1
Calculated lattice parameters (a, b and c), volume (V), bulk modulus (B_0), and its pressure derivative (B_0') along with the experiments [16].

	PBE	IVDW1	IVDW12	IVDW11	Expt.
$a = b$ (Å)	4.65	4.09	4.28	4.31	4.35
c (Å)	14.73	14.14	13.78	13.88	13.71
V (Å^3)	319.27	237.32	252.17	258.44	260.01
B_0 (GPa)	–	–	–	15.3	18.1
B_0' (GPa)	–	–	–	8.6	2.0

as the most stable at zero pressure. Table 1 lists the unit-cell parameters that were determined. According to our findings, the DFT-D3 approach of Grimme, which includes van der Waals interactions [34], yields a better prediction of the crystal structure of AuI. At 0 GPa and 0 K, the computed unit-cell parameters are $a = b = 4.31$ Å, and $c = 13.88$ Å, which correlate well with experiments performed at ambient conditions [16]. Wyckoff locations 4d (0, 0, 0) and 4e (0, 0, z) correspond to the *Au* and *I* atoms, respectively. The calculated z coordinate for *I* is 0.1530, which is consistent with experiments ($z = 0.1551$). The crystal structure is formed by layers of −I−Au−I−Au−I− polymeric zigzag chains, where the *Au−I−Au* angle is 70.63°. The layers are stacked along the *c*-axis linked by weak van der Waals interactions among *I* atoms, as shown in Fig. 1.

Au and *I* atoms are covalently bound in AuI, and the infinite zigzag chains are joined along the *ab*-plane by *Au⋯Au* aurophilic interactions. The measured interatomic lengths are compared to the results of the experiments in Table 2. The intralayer *Au−I* bond distances are the shortest distances measuring 2.639 Å. Each layer contains an *fcc*-like square 2D network of *Au* atoms, where the bond distance between *Au* atoms is 3.051 Å. This bond distance, which is

Table 2
Calculated bond lengths in comparison with the experiments [16].

Bond lengths (Å)	Calculations	Expt.
Au−I	2.64	2.60
Au−Au	3.05	3.08
I−I (Interlayer)	4.03	4.07
I−I (Intralayer)	4.31	4.36

equivalent to $a/\sqrt{2}$, is typical of aurophilic bonds [41,42]. Similar to the *Au* atoms in each layer, *I* atoms form square 2D networks on either side of the *Au* network, and the distance between these intralayer *I* atoms is eqivalent to the unit-cell parameter *a*. In contrast, the interlayer *I* atoms are sitting at the regular square pyramidal sites with bond distances of 4.032 Å. We've also calculated the charge density in the [010] direction. Fig. S1 (in supporting information) depicts this. Due to the difference in electronegativity between the *Au* and *I* atoms (*Au* = 2.54, *I* = 2.66), the figure suggests a covalent bonding between atoms.

We computed the pressure dependency of all structural parameters to examine the impact of pressure on structural properties. The volume (V/V_0) and normalised unit cell parameters (a/a_0, c/c_0) correspond well with experiments [16] [see Fig. S2(a) in supporting information]. A third-order Birch-Murnaghan equation of state [37] accurately characterises the fluctuation in unit-cell volume as a function of pressure [see Fig. S2(b) in supporting information]. The bulk modulus, B_0, and its pressure derivative, B_0', at 0 GPa are 15.3 GPa and 8.6, respectively. With the increase in pressure, the *Au−I−Au* angle decreases from 70.63° to 69.49° at 7 GPa [see Fig. S3(a) in supporting information]. In prior research, information on bond distances up to 3.3 GPa was only available [16]. Bond distances follow a similar pattern in our calculations, but the conclusions are only valid up to 7 GPa, the theoretical amorphization pressure (see next section). As shown in Fig. S3(b) (in supporting information), covalent *Au−I* bonds are less compressible than *Au−Au* and *I−I* bonds. The interlayer van der Waals *I−I* bonds are the most compressible.

3.2. Elastic and mechanical properties

The elastic constants (C_{ij}) of solids provide information about interatomic interactions of solids, mechanical stability, ductile/brittle nature, strength, hardness, and stiffness in solids [43,44]. Strain-stress relationships [45], as implemented in DFT, are used to determine the elastic constants. The following prerequisites for Born stability in a tetragonal structure must be met. [46,47]:

$$M_1 = C_{11} > 0, \ M_2 = C_{33} > 0,$$

$$M_3 = C_{44} > 0, \ M_4 = C_{66} > 0,$$

$$M_5 = C_{11} - C_{12} > 0, \ M_6 = C_{11} + C_{33} - 2C_{13} > 0,$$

$$M_7 = 2(C_{11} + C_{12}) + C_{13} + 4C_{13} > 0$$

Table 3 lists the six independent elastic constants derived at zero pressure. They satisfy all the stability criteria. The elastic constants C_{11} and C_{33} denote linear compression resistance in the *a*- and *c*-direction, respectively. C_{12}, C_{13}, C_{44}, and C_{66}, the other independent constants, are related to shape elasticity [48]. C_{33} is greater than C_{11}, suggesting that AuI should be more compressible along the *a*-axis than along the *c*-axis, as demonstrated by previous research [16]. The tetragonal system provides two Cauchy relations such as C_{12} = C_{66} and C_{33} = C_{44} [46]. The results of our calculations do not satisfy these two relations, indicating the presence of the non-central forces in AuI due to its partial covalent nature [49].

The elastic moduli for AuI, such as the bulk (B) and shear modulus (G), were calculated using the Voigt-Reuss-Hill technique [50–52]. Young's modulus (E) and Poisson's ratio (ν) have been determined in addition to B and G [53]. Table 4 provides a summary of

Table 3
Calculated elastic constants (C_{ij} in GPa) for AuI at zero pressure and zero temperature.

C_{11}	C_{12}	C_{13}	C_{33}	C_{44}	C_{66}
24.76	10.77	13.44	26.77	4.76	7.09

Table 4
Calculated elastic moduli (B, G and E, in GPa), Poisson's ratio (ν), B/G Ratio, Vickers hardness (H_V, in GPa), and shear anisotropy factors (A_1 and A_3).

B	G	E	ν	B/G	H_V	A_1	A_3
16.90	5.80	15.60	0.35	2.90	0.95	0.77	1.01

the determined mechanical characteristics. The value of B_0 found using the Birch-Murnaghan equation of state is comparable to the bulk modulus calculated using the elastic constants. Its value of 15.3–16.9 GPa indicates that AuI is highly compressible, being more compressible than several metal-organic framework compounds [54]. Pugh's B/G ratio [55] can be utilised to assess if a material is ductile or brittle. If the B/G ratio is more than 1.75, the material is termed ductile; otherwise, it will exhibit brittle behaviour. In our case, the B/G (= 2.90) is more than 1.75, indicating that AuI is ductile. The ductile or brittle nature of a material can also be determined from the Frantsevich's rule [56]. It states that the material is ductile for a Poisson's ratio (ν) larger than 0.26. The present value of ν confirms the ductile nature of AuI.

Another relevant mechanical property is the Vickers hardness (H_V) which can be correlated with bulk modulus and shear modulus [57]. AuI is classed as a soft material based on the computed value. We have also obtained the shear anisotropic factors A_1 and A_3. They reflect the bonding nature in different crystallographic directions and provide information about microcrack formation in materials [58]. A_1 and A_3 correspond to the (100)/(010) and (001) planar shear anisotropies, respectively. In our case, A_1 is 30 % smaller than A_3, indicating an anisotropic response to deformations.

The Debye temperature (θ_D) is a critical parameter that affects a variety of physical properties, including lattice vibrations, phonons, specific heat, melting point, and thermal expansion. The higher value of the Debye temperature indicates the higher phonon thermal conductivity [59]. The θ_D can be determined from the average sound velocity (v_m). We have estimated it from the longitudinal (v_l) and transverse (v_t) sound velocities determined from the elastic moduli [60]. The derived parameters are summarised in Table 5. We also included the melting temperature obtained the relationship proposed by Fine [61] for intermetallic compounds (including AuCd and AuZn): $T_m = 354 + 4.5\left(\frac{2C_{11} + C_{33}}{3}\right)$. The obtained melting temperature, 468 K, is consistent with experiments [16], which found that AuI decomposes at 393 K before melting. Additionally, we have also calculated Grüneisen parameter (γ), one of the most valuable quantities in thermodynamics, in terms of the Poisson ratio [62]: $\gamma = \frac{3}{2}\left(\frac{1+\nu}{2-3\nu}\right)$. The Grüneisen parameter has a higher value than other compounds such as CsCl, CsBr, and CsI [62]. This high value of Grüneisen parameter gives us a hint about presence of anharmonicity in the system.

3.3. Mechanical stability at high pressure

To study the pressure-driven structural changes in AuI, we have performed calculations at 0 K up to 7 GPa. Under hydrostatic pressure (P), the elastic constants (C_{ij}) become inadequate to maintain the stability of the compound and must be substituted with elastic stiffness constants (B_{ij}). For a tetragonal system the elastic stiffness constants are: $B_{11} = C_{11} - P$, $B_{12} = C_{12} - P$, $B_{13} = C_{13} + P$, $B_{33} = C_{33} - P$, B_{44}

Table 5
Density (ρ), longitudinal (v_l), transverse (v_t), and average (v_m) wave velocities, Debye temperature (θ_D), melting temperature (T_m), and Grüneisen parameter (γ) at zero pressure.

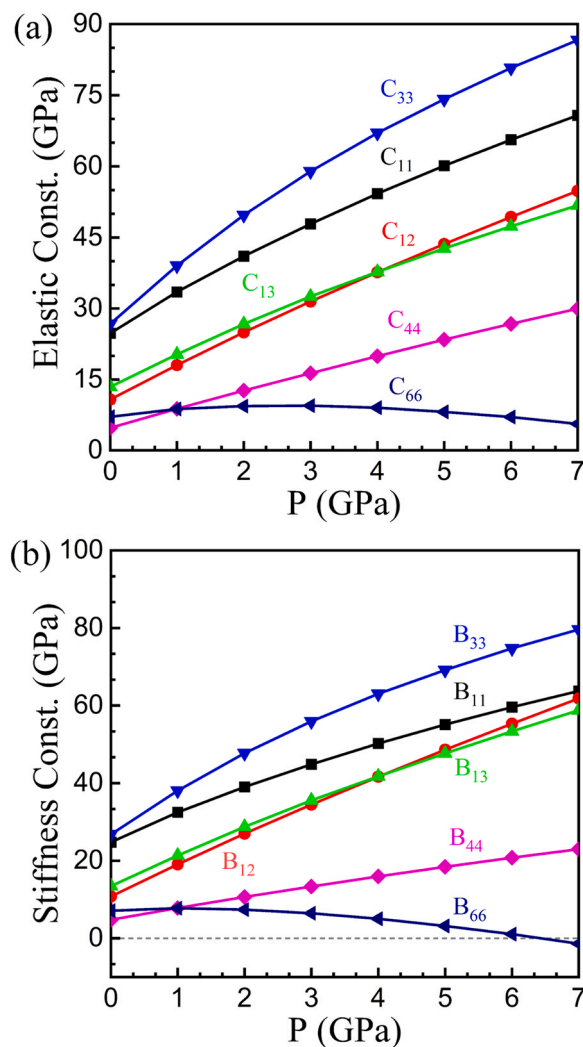| ρ (gr/cc)	v_l (km/s)	v_t (km/s)	v_m (km/s)	θ_D (K)	T_m (K)	γ
8.32	1.72	0.84	0.94	87.72	468	2.09

Fig. 2. Pressure dependence of (a) elastic constants and (b) elastic stiffness constants.

= C_{44} - P, B_{66} = C_{66} – P [63]. The Born stability criteria are unchanged while using these elastic stiffness constants. The variations of elastic constants and elastic stiffness constants in response to pressure are depicted in Fig. 2 and Tables S1 and S2 (in supporting information). The expected response to compression is an increase in the elastic constant values. All the elastic stiffness constants in AuI increase with pressure, except for B_{66}, which declines and reaches negative about 7 GPa.

According to the stability criterion of Born (as mentioned above), the M_4 stability criterion is violated. Notice that M_4 is related to a pure shear instability. On the other hand, M_5, which is related to the tetragonal shear moduli, is also found to be negative at ~8 GPa. According to our DFT study of AuI, we anticipate that a mechanical instability occurs at around ~7 GPa, and that PIA may arise owing to the start of shear instability at this pressure. Notice the ambient pressure structure is the thermodynamically stable phase of AuI. This is supported by the fact that XRD patterns show the appearance of additional XRD peaks at 3.8 GPa indicating the onset of a transition [16], but the phase transition is never completed up to the pressure where the tetragonal structure of AuI becomes mechanically unstable, 7 GPa. Then we considered that the combination of kinetic barriers blocking the solid-solid transition and the mechanical instability that we found causes the final collapse of the crystal structure. This yield to the amorphous phase observed in
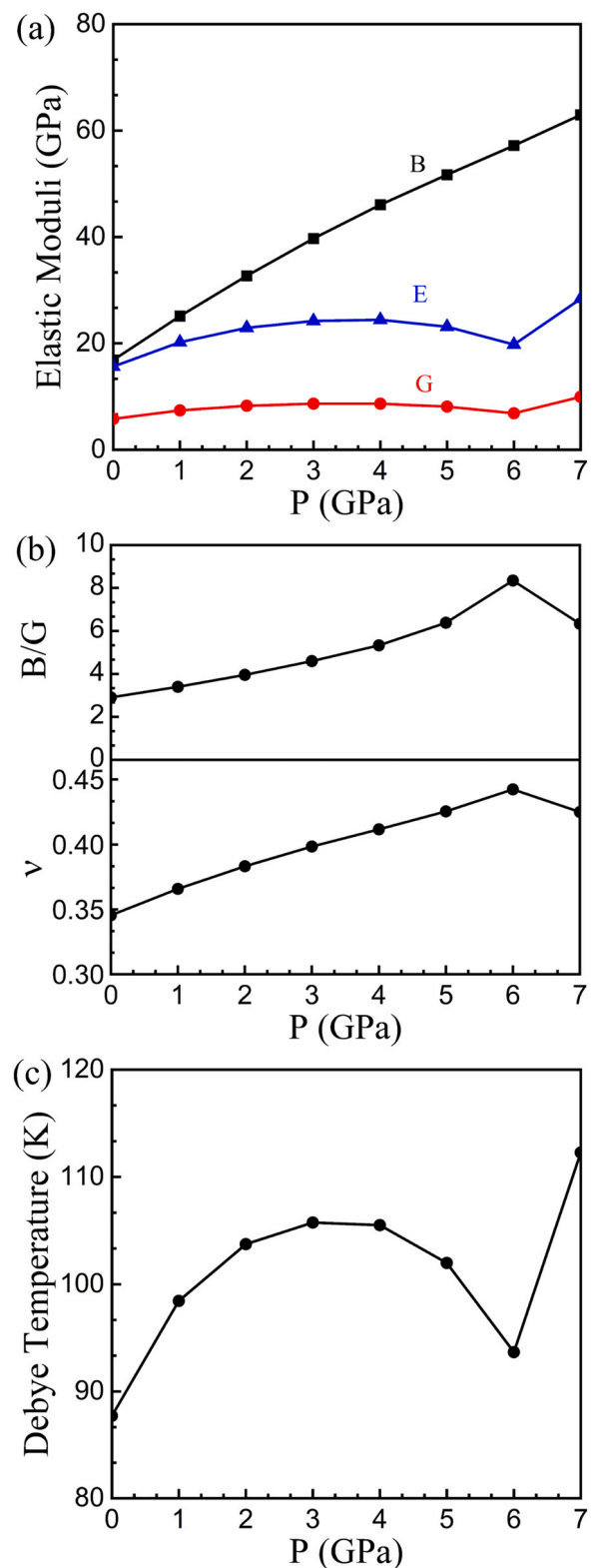

Fig. 3. Pressure dependence of (a) Elastic moduli, (b) Poisson's ratio and B/G values, and (c) Debye temperature.

experiments [64,65]. In the next section, we will provide information showing that the elastic softening is related to a phonon softening.

For theoretical comprehensiveness, we have plotted the variation of elastic moduli versus pressure [see Fig. 3 and Tables S3–S5 in supporting information]. Young's modulus, shear modulus, and

Debye temperature exhibit a non-linear behaviour up to 6 GPa and a rapid transition from 6 to 7 GPa, although the bulk modulus increases as pressure increases. The Poisson's ratio increases up to 6 GPa and then declines until it reaches 7 GPa. All these elastic moduli magnitudes abruptly change behaviour around 7 GPa, suggesting that the crystal structure is destabilised. We've also discovered that when pressure increases, the Vickers hardness rapidly decreases [see Table S4 in supporting information]. The decrease in hardness implies that AuI becomes softer as pressure increases. This encourages the disintegration of materials under pressure, which can lead to amorphization. We observe an increase in the B/G ratio with pressure, which indicates the enhancement in the ductility of the compound under pressure.

The shear anisotropic value A_1 increases with the application of pressure, but A_3 shows a fluctuation in its values with pressure resulting in the compound's overall anisotropic behaviour even at high pressures [see Table S4 in supporting information]. At 7 GPa, A_3 becomes negative. This unphysical result confirms that the crystal structure of AuI is not stable for $P > 7$ GPa. On the other hand, the longitudinal sound velocity has been found to increase as pressure increases up to 7 GPa. In contrast, the transverse sound velocity exhibits an unusual behaviour under high pressure with a discontinuity at 7 GPa, as shown in Table S5 (in supporting information). For the sake of completeness, we have also included the melting curve and pressure dependence of the Grüneisen parameter in the supporting information. An increase in the value of the Grüneisen parameter with respect to pressure causes an increase in anharmonicity in the system, resulting in imaginary phonon modes (as will be described in the upcoming section).

3.4. Phonon calculations

We have also studied the dynamical stability of AuI under pressure to explore its possible relation to amorphization. We have determined the phonon dispersion along the high-symmetry points, as shown in the irreducible Brillouin zone Fig. 1(d), at zero and 7 GPa pressure. They are shown in Fig. 4. We discovered that all phonon branches exist within the positive frequency domain at ambient conditions [see Fig. 4(a)], demonstrating that the tetragonal structure of AuI is dynamically stable. In contrast, not all phonon branches exist within the positive frequency domain at 7 GPa [see Fig. 4(b)] indicating a dynamical instability, a fact that will be discussed in more detail towards the end of this section.

A mode analysis was carried out to learn more about the vibrational spectra of ambient structure. According to group theory, AuI has 24 vibrational modes; 3 are acoustic modes ($2E_u+A_{2u}$) and the rest are the optical modes ($8E_u+3B_{1u}+4E_g+2A_{2u}+1B_{2u}+1A_{1u}+1B_{2g}+1A_{1g}$).

Calculated mode frequencies are provided in Table S6 in supporting information. The infrared (IR) active modes are $8E_u+B_{1u}+2A_{2u}+1B_{2u}+1A_{1u}$ and the Raman active modes are $4E_g+1B_{2g}+1A_{1g}$. A thorough examination of various vibrations associated with phonon spectrum has been carried out. The atomic movement associated with each mode is depicted in Fig. S5 in supporting information. The acoustic modes are the vibrations of the entire molecule in three separate directions at near to zero frequencies. The IR mode at frequency 16.45 cm^{-1} is due to rocking vibration of AuI molecule as a whole, whereas the IR mode at frequency 26.12 cm^{-1} is the resultant of individual scissoring of atoms and symmetric stretching vibrations of the whole molecule. Fig. S5(d) in supporting information shows the Raman mode at frequency 29.79 cm^{-1}, where only *I* atoms show wagging vibrations. Fig. S5(e) and (f) in supporting information show the IR mode at frequencies 40.65 cm^{-1} and 45.30 cm^{-1}, where the former shows a rocking vibration, and the latter shows alternate rocking and wagging vibrations. The IR mode with frequency 52.52 cm^{-1} shows scissoring vibrations of *Au* and *I*
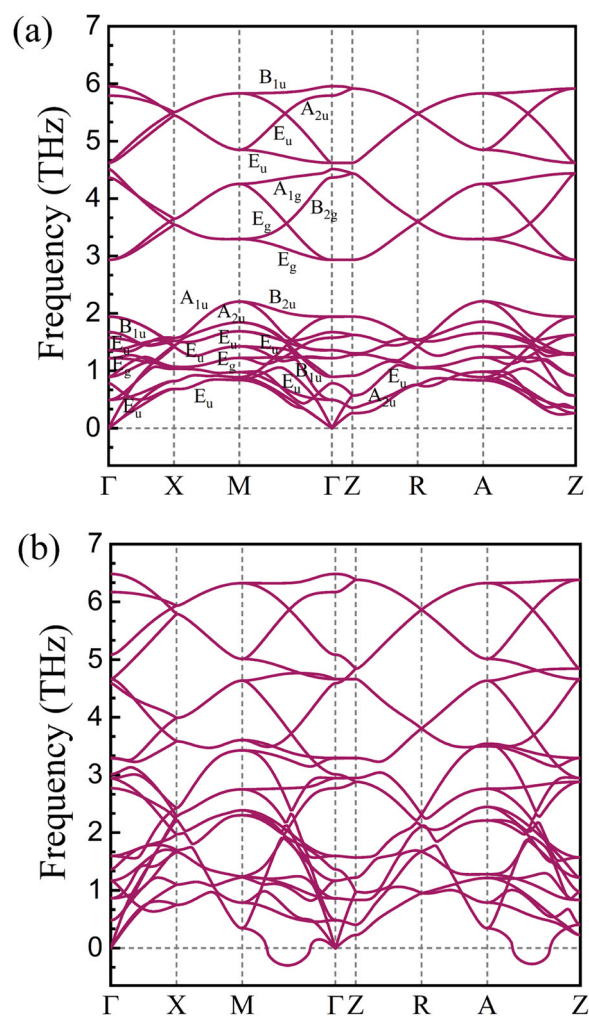

Fig. 4. Phonon dispersion curves at (a) zero pressure and (b) 7 GPa pressure.

atoms. In the IR mode with frequency 64.73 cm^{-1}, shown in Fig. S5(h) in supporting information, only *Au* atoms shows twisting vibrations whereas in the Raman mode with frequency 97.83 cm^{-1}, shown in Fig. S5(i) in supporting information, only *I* atoms shows stretching vibrations. Both the modes with 145.62 cm^{-1} and 198.64 cm^{-1} frequencies have stretching vibrations. Finally, the IR mode shown in Fig. S5(k) in supporting information with frequency 154.19 cm^{-1} have both silent and asymmetric stretching vibrations in alternate layers.

High-pressure calculations of these vibrational spectra have been carried out at 7 GPa, where few modes are becoming negative, as shown in Fig. 4(b). The presence of imaginary phonon modes indicates that the compound becomes dynamical unstable. Around 7 GPa, amorphization is favoured by both dynamical and mechanical instabilities [65].

The vibrational modes that we believe trigger the dynamical instability of the compound have also been investigated. The soft mode is a doubly degenerate acoustic mode (E_u), which involves rigid translations of layers formed by −I−Au−I−Au−I− polymeric zigzag chains, as shown in Fig. 5. At zero pressure, all atoms are vibrating parallel to each other along. However, at 7 GPa, all atoms vibrate in some tilting manner. It indicates that, a disorder is developed within the layers forming AuI. This fact is expected to cause a shear instability, which could result in the amorphization of AuI under high-pressure. In summary, we propose that AuI, because of its peculiar crystal structure accommodate stresses by means of atomic displacements which result in a subsequent loss of
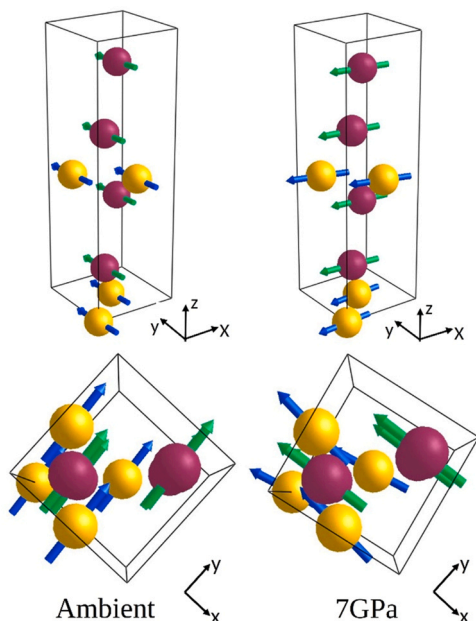
Fig. 5. Acoustic doubly degenerate mode (E$_u$) of AuI at 0 and 7 GPa (yellow and purple colour represent *Au* and *I* atoms, respectively).

translational periodicity. This fact, results in the transformation to a frustrated non-crystalline solid [66,67] as we described in Section 3.3.

3.5. Electronic properties

Subsequently, we have computed the electronic structure calculations for AuI using the GGA exchange and correlation functionals. The calculated bandgap is 1.42 eV, as shown in Fig. 6(a). However, as GGA underestimates the bandgap, we have included the HSE exchange and correlation functional to improve it. As illustrated in Fig. 7, the bandgap obtained by using HSE exchange and correlation functionals is 2.31 eV. The band structure plots indicate that the given compound is a semiconductor with an indirect bandgap. To understand more about the electronic structure of AuI, we plotted the total and partial density of states at ambient pressure in Fig. 6(b). The contribution of *Au* atoms dominates the valence band at the Fermi level, but both *Au* and *I* atoms contribute equally to the conduction band. The crystal structure of our investigated system is non-symmorphic with a preserved inversion symmetry. It contains time-reversal symmetry (TRS) and a four-fold (screw) rotation symmetry about the *z*-axis. Consequently, the electronic band structure displays several non-trivial band features, as shown in Fig. 6(a). The presence of TRS and inversion symmetry along X-M and Z-R-A path, enforces two-fold degeneracy in all bands along these paths.

Interestingly, bands along the Z-R-A path are merging at points R and A, forming Dirac-like dispersions with four-fold degeneracy. The role of SOC becomes more significant in such cases, so we have included the same in calculations. Fig. 8(a) displays the band structure properties with SOC. The bands away from the Z-R-A path are two-fold degenerate, merging at points Z and R, and enabling four-fold degeneracy at these points. We observed four connected bands forming Dirac-like band crossings along path Z-R. These four sets of bands connect two energy levels at Z and R in a zigzag manner, and form an hourglass dispersion, which is shown in Fig. 8(c). Here Z and R are linked by U, providing two energy level splitting in U, where U = (0, ν, 0.5) [68]. The hourglass band crossings can only appear in high-symmetry line (HSL) or high-symmetry plane (HSPL) for which two different irreducible representations (irreps) are allowed [69].
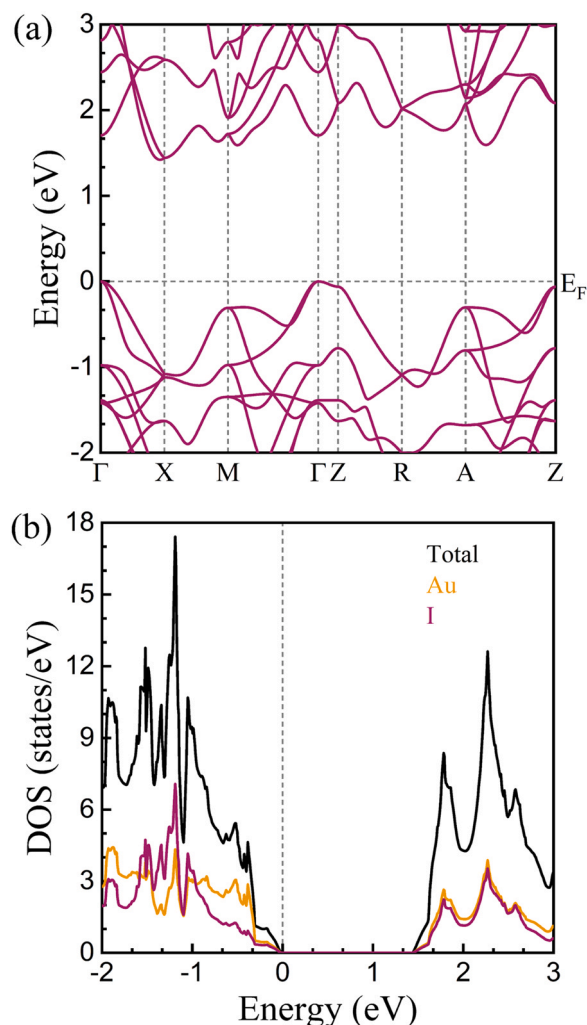

Fig. 6. (a) The electronic band structure (with GGA) in the absence of SOC, and (b) the projected density of states (PDOS) of AuI.
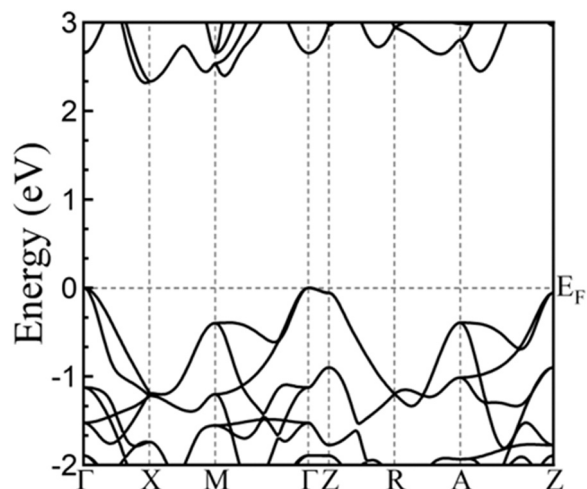

Fig. 7. (a) The electronic band structure calculated using HSE functionals in the absence of SOC. For completeness calculations including SOC are given in Fig. S6 in supporting information.

The observed irreps corresponding to Z and R points are labelled in Fig. 8(c). We can see that there is a four-fold crossing on the high-symmetry line U, which connects Z and R. The irreps of U include
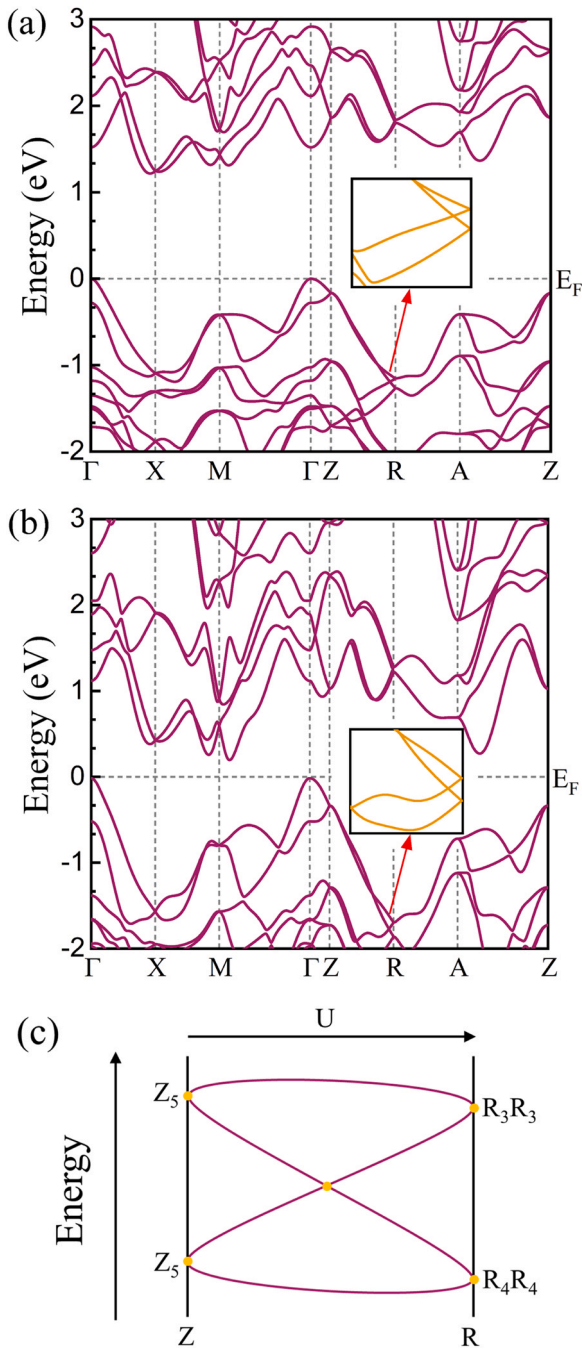
Fig. 8. (a) The electronic band structure (with GGA) at ambient and (b) 7 GPa in the presence of SOC (Dirac point with hourglass dispersion bands are shown in inset), and (c) schematic figure showing the hourglass dispersion along an arbitrary path on the $k_z = \pi$ plane connecting Z to the point R.
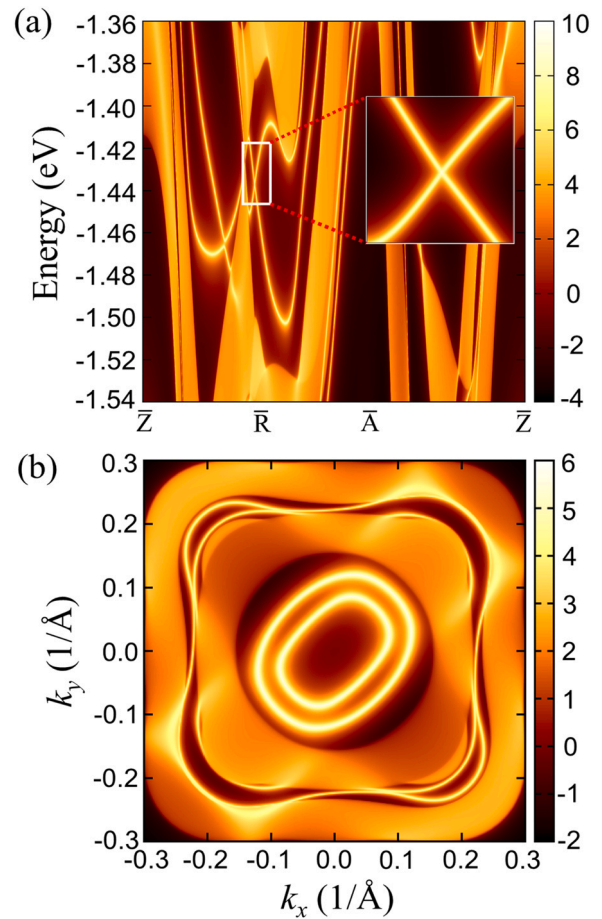

Fig. 9. (a) The surface states with I termination along Z-R-A-Z path, where the inset plot indicates the Dirac point, and (b) the Fermi arcs with connecting the projections of Dirac points on the (001) surface.

four irreps U_2, U_3, U_4 and U_5. In addition, there are two irreps R_3R_3 (paired by TRS) and R_4R_4 at point R, and one irrep Z_5 at point Z. According to the compatibility relations [68], the irreps at Z are found to be related with the irreps at U as follows:

$$Z_5 \rightarrow U_2U_4 \oplus U_3U_5$$

In addition, for R.

$$R_3R_3 \rightarrow 2\,U_2U_4 \text{ and } R_4R_4 \rightarrow 2\,U_3U_5$$

Hence the splitting patterns can be denoted as $U_2U_4 \oplus U_3U_5$, $U_2U_4 \oplus U_3U_5$; $2\,U_2U_4$, $2\,U_3U_5$. We can see that U_2U_4 and U_3U_5 have

been interchanged between Z and R. As we can see that, the irreps of the top and bottom parts are different but share the same irreps at the neck parts, which indicates it to be a type-A hourglass dispersion [69]. The above relations satisfy the requirements of type-A hourglass band crossings along Z-R path in AuI, which is similar to AuBr [22].

The four-fold degeneracy is observed along path R to A also. This analysis of bulk band crossings motivates us to explore more about the topological nature in AuI at ambient pressure. Therefore, we have plotted the surface states with I termination along the $k_z = 0.5$ plane [as shown in the Brillouin zone schematic Fig. 1(d)] to confirm these crossings [see Fig. 9(a)]. Dirac-like band dispersion is seen in the surface state also. The surface Fermi arcs are also displayed in Fig. 9(b).

In Fig. 9, one can observe that the Fermi arcs connect the projections of movable Dirac point and form a Dirac loop. The Dirac point in hourglass dispersion under SOC is protected by C_{2y} screw-rotation symmetry. AuI possesses movable Dirac points forming hourglass dispersions as reported for AuBr previously [22]. To check the trivial or non-trivial topology in AuI, we have calculated the Z_2 invariants. The calculated value of Z_2 invariants are (0; 0 1 0). The Z_2 invariants and Dirac point are the evidence to claim AuI as a weak non-trivial topological material.

The electronic structure under pressure is also studied using the GGA exchange and correlation functionals, and the pressure-dependent bandgap is plotted in Fig. S7 in supporting information. The bandgap decreases with an increase in pressure and remains an indirect bandgap. In addition, the bandgap at 7 GPa pressure is

0.54 eV. The decrease in band gap results from amorphization due to the structural disorder. In this case, we found the transformation of a crystalline semiconductor to an amorphous semiconducting phase without a band gap closure. We have also analysed the electronic band structure with the inclusion of SOC under high pressure [see Fig. 8(b)]. The four-fold degenerate bands (Dirac point) along Z-R path with hourglass dispersions can also be seen up to amorphization, making it a robust topological material.

4. Conclusions

Using density-functional theory, we present a comprehensive, methodical analysis of the underlying mechanical, dynamical, and electronic properties of AuI at ambient and high pressure. Experiments and the estimated structural and mechanical properties agree well. According to our computation, AuI amorphizes under high pressure. At 7 GPa, mechanical and dynamical instabilities arise in AuI, triggering amorphization. In the light of vibrational mode examination at ambient and high pressure, the softening of acoustic modes under pressure leads to amorphization. With the inclusion of spin-orbit coupling, the electronic properties uncover the presence of a movable Dirac point with hourglass bands dispersion along the band path Z-R, which remains robust up to amorphization. Our calculations give a more profound knowledge in understanding the properties of AuI.

CRediT authorship contribution statement

Kanchana Venkatakrishnan, Ganapathy Vaitheeswaran and **Daniel Errandonea** designed the project. **Kanchana Venkatakrishna**n and **Ganapathy Vaitheeswaran** proposed the framework of the computational approach, **Jaspreet Singh** and **Sushree Sarita Sahoo** performed the calculations. All authors analysed the data and wrote the manuscript.

Data availability

Data will be made available on request.

Declaration of Competing Interest

The authors declare the following financial interests/personal relationships which may be considered as potential competing interests: Daniel Errandonea reports financial support was provided by Ministry of Science and Investigation of Spain.

Acknowledgements

Appendix A. Supporting information

Supplementary data associated with this article can be found in the online version at doi:10.1016/j.jallcom.2022.167178.

References

[1] P.F. McMillan, New materials from high-pressure experiments, Nat. Mater. 1 (2002) 19–25.

[2] M.H. Cohen, J. Íñiguez, J.B. Neaton, Flat branches and pressure amorphization, J. Non Cryst. Solids 307 (2002) 602–612.

[3] R.J. Hemley, A.P. Jephcoat, H.K. Mao, L.C. Ming, M.H. Manghnani, Pressure-induced amorphization of crystalline silica, Nature 334 (1988) 52–54.

[4] A.K. Arora, T. Sakuntala, The role of orientational disorder in the pressure-induced amorphization of lithium potassium sulphate, J. Phys. Condens. Matter 4 (1992) 8697.

[5] K. Fuchizaki, S. Sugiyama, Y. Fujii, Search for precursor of pressure-induced amorphization of molecular crystal SnI$_4$: thermodynamic stability of low-pressure crystalline phase, J. Chem. Phys. 112 (2000) 10379–10390.

[6] O. Mishima, L.D. Calvert, E. Whalley, "Melting ice" i at 77 K and 10 kbar: a new method of making amorphous solids, Nature 310 (1984) 393–395.

[7] M. Misawa, F. Shimojo, First-principles study of pressure-induced amorphization of Fe$_2$SiO$_4$ fayalite, Phys. Status Solidi B 257 (2020) 2000173.

[8] T.R. Ravindran, A.K. Arora, T.A. Mary, High pressure behavior of ZrW$_2$O$_8$: Grüneisen parameter and thermal properties, Phys. Rev. Lett. 84 (2000) 3879.

[9] A. Jayaraman, S.Y. Wang, S.K. Sharma, Pressure-induced amorphization in NaLa (MoO$_4$)$_2$; A high pressure Raman and IR absorption study, Solid State Commun. 93 (1995) 885–890.

[10] P. Richet, P. Gillet, Pressure-induced amorphization of minerals: a review, Eur. J. Miner. (1997) 907–934.

[11] R.R. Winters, G.C. Serghiou, W.S. Hammack, Observation and explanation of the reversible pressure-induced amorphization of Ca(NO$_3$)$_2$/NaNO$_3$, Phys. Rev. B 46 (1992) 2792.

[12] J.S. Tse, D.D. Klug, Anisotropy in the structure of pressure-induced disordered solids, Phys. Rev. Lett. 70 (1993) 174.

[13] T. Sakuntala, A.K. Arora, N.V.C. Shekar, P.C. Sahu, Orientational disorder: a mechanism of amorphization at high pressure, Europhys. Lett. 44 (1998) 728.

[14] O. Mishima, L.D. Calvert, E. Whalley, An apparently first-order transition between two amorphous phases of ice induced by pressure, Nature 314 (1985) 76–78.

[15] J.S. Tse, D.D. Klug, Mechanical instability of -quartz: a molecular dynamics study, Phys. Rev. Lett. 67 (1991) 3559.

[16] V. Monteseguro, D. Errandonea, S.N. Achary, J.A. Sans, F.J. Manjón, S. Gallego-Parra, C. Popescu, Structural Characterization of aurophilic gold(I) Iodide under high pressure, Inorg. Chem. 58 (2019) 10665–10670.

[17] D. Errandonea, D. Martínez-García, A. Segura, J. Haines, E. Machado-Charry, E. Canadell, J.C. Chervin, A. Chevy, High-pressure electronic structure and phase transitions in monoclinic InSe: X-ray diffraction, Raman spectroscopy, and density functional theory, Phys. Rev. B 77 (2008) 045208.

[18] S. Hull, D.A. Keen, Pressure-induced phase transitions in AgCl, AgBr, and AgI, Phys. Rev. B 59 (1999) 750–761.

[19] D. Santamaría-Pérez, D. Daisenberger, J. Ruiz-Fuertes, T. Marqueño, R. Chulia-Jordan, C. Muehle, M. Jansen, P. Rodriguez-Hernandez, A. Muñoz, E.R. Johnson, A. Otero-De-La-Roza, Gold(i) sulfide: unusual bonding and an unexpected computational challenge in a simple solid, Chem. Sci. 10 (2019) 6467–6475.

[20] T. Söhnel, H. Hermann, P. Schwerdtfeger, Solid state density functional calculations for the group 11 monohalides, J. Phys. Chem. B 109 (2005) 526–531.

[21] R.M. Sattigeri, T.K. Gajaria, P.K. Jha, P. Śpiewak, K.J. Kurzydłowski, Emergence of -s, -p-d band inversion in zincblende gold iodide topological insulator and its thermoelectric properties, J. Phys. Condens. Matter 33 (2021) 155402.

[22] M.M. Hirschmann, A. Leonhardt, B. Kilic, D.H. Fabini, A.P. Schnyder, Symmetry-enforced band crossings in tetragonal materials: Dirac and Weyl degeneracies on points, lines, and planes, Phys. Rev. Mater. 5 (2021) 054202.

[23] X. Wan, A.M. Turner, A. Vishwanath, S.Y. Savrasov, Topological semimetal and Fermi-arc surface states in the electronic structure of pyrochlore iridates, Phys. Rev. B 83 (2011) 205101.

[24] T. Bzdušek, Q.S. Wu, A. Rüegg, M. Sigrist, A.A. Soluyanov, Nodal-chain metals, Nature 538 (2016) 75–78.

[25] Q. Wang, Y. Xu, R. Lou, Z. Liu, M. Li, Y. Huang, D. Shen, H. Weng, S. Wang, H. Lei, Large intrinsic anomalous Hall effect in half-metallic ferromagnet Co$_3$Sn$_2$S$_2$ with magnetic Weyl fermions, Nat. Commun. 9 (2018) 1–8.

[26] B. Skinner, L. Fu, Large, nonsaturating thermopower in a quantizing magnetic field, Sci. Adv. 4 (2018) 2621.

[27] K. Fukushima, D.E. Kharzeev, H.J. Warringa, Chiral magnetic effect, Phys. Rev. D 78 (2008) 074033.

[28] M.Z. Hasan, C.L. Kane, Colloquium: topological insulators, Rev. Mod. Phys. 82 (2010) 3045.

[29] M.G. Vergniory, L. Elcoro, C. Felser, N. Regnault, B.A. Bernevig, Z. Wang, Author correction: a complete catalogue of high-quality topological materials, Nature 566 (2019) 480–485.

[30] G. Kresse, J. Furthmüller, Efficiency of ab-initio total energy calculations for metals and semiconductors using a plane-wave basis set, Comput. Mater. Sci. 6 (1996) 15–50.

[31] J.P. Perdew, K. Burke, M. Ernzerhof, Generalized gradient approximation made simple, Phys. Rev. Lett. 77 (1996) 3865.

[32] H.J. Monkhorst, J.D. Pack, Special points for Brillouin-zone integrations, Phys. Rev. B 13 (1976) 5188.

[33] S. Grimme, Semiempirical GGA-type density functional constructed with a long-range dispersion correction, J. Comput. Chem. 27 (2006) 1787–1799.

[34] S. Grimme, J. Antony, S. Ehrlich, H. Krieg, A consistent and accurate ab initio parametrization of density functional dispersion correction (DFT-D) for the 94 elements H-Pu, J. Chem. Phys. 132 (2010) 154104.

[35] S. Grimme, S. Ehrlich, L. Goerigk, Effect of the damping function in dispersion corrected density functional theory, J. Comput. Chem. 32 (2011) 1456–1465.

[36] X. Gonze, C. Lee, Dynamical matrices, Born effective charges, dielectric permittivity tensors, and interatomic force constants from density-functional perturbation theory, Phys. Rev. B 55 (1997) 10355.

[37] F. Birch, Finite elastic strain of cubic crystals, Phys. Rev. 71 (1947) 809–824.

[38] G. Pizzi, V. Vitale, R. Arita, S. Blügel, F. Freimuth, G. Géranton, M. Gibertini, D. Gresch, C. Johnson, T. Koretsune, J. Ibañez-Azpiroz, H. Lee, J.M. Lihm, D. Marchand, A. Marrazzo, Y. Mokrousov, J.I. Mustafa, Y. Nohara, Y. Nomura, L. Paulatto, S. Poncé, T. Ponweiser, J. Qiao, F. Thöle, S.S. Tsirkin, M. Wierzbowska, N. Marzari, D. Vanderbilt, I. Souza, A.A. Mostofi, J.R. Yates, Wannier90 as a community code: new features and applications, J. Phys. Condens. Matter 32 (2020) 165902.

[39] Q.S. Wu, S.N. Zhang, H.F. Song, M. Troyer, A.A. Soluyanov, WannierTools: an open-source software package for novel topological materials, Comput. Phys. Commun. 224 (2018) 405–416.

[40] M.P. Lopez Sancho, J.M. Lopez Sancho, J. Rubio, Highly convergent schemes for the calculation of bulk and surface Green functions, J. Phys. F Met. Phys. 15 (1985) 851.

[41] A. Vegas, Cations in inorganic solids, Cryst. Rev. 7 (2000) 189–283.

[42] H. Schmidbaur, The aurophilicity phenomenon: a decade of experimental findings, theoretical concepts and emerging applications, Gold. Bull. 33 (2000) 3–10.

[43] D. Errandonea, C. Ferrer-Roca, D. Martínez-Garcia, A. Segura, O. Gomis, A. Muñoz, P. Rodríguez-Hernández, J. López-Solano, S. Alconchel, F. Sapiña, High-pressure x-ray diffraction and ab initio study of Ni$_2$Mo$_3$N, Pd$_2$Mo$_3$N, Pt$_2$Mo$_3$N, Co$_3$Mo$_3$N, and Fe$_3$Mo$_3$N: Two families of ultra-incompressible bimetallic interstitial nitrides, Phys. Rev. B 82 (2010) 174105.

[44] E. Ateser, H. Ozisik, K. Colakoglu, E. Deligoz, The structural and mechanical properties of CdN compound: a first principles study, Comput. Mater. Sci. 50 (2011) 3208–3212.

[45] Y. le Page, P. Saxe, Symmetry-general least-squares extraction of elastic data for strained materials from ab initio calculations of stress, Phys. Rev. B 65 (2002) 104104.

[46] M. Born, K. Huang, M. Lax, Dynamical theory of crystal lattices, Am. J. Phys. (1955).

[47] S. Piskunov, E. Heifets, R.I. Eglitis, G. Borstel, Bulk properties and electronic structure of SrTiO$_3$, BaTiO$_3$, PbTiO$_3$ perovskites: an ab initio HF/DFT study, Comput. Mater. Sci. 29 (2004) 165–178.

[48] X. Gao, Y. Jiang, R. Zhou, J. Feng, Stability and elastic properties of Y-C binary compounds investigated by first principles calculations, J. Alloy. Compd. 587 (2014) 819–826.

[49] E. Karaca, E. Arslan, H.M. Tütüncü, G.P. Srivastava, Physical properties of the body-centred tetragonal, Philos. Mag. 97 (2017) 1866–1883.

[50] F. Wille, Die Mathematik im Verlag B.G. Teubner, in: Wechselwirkungen: Der Wissenschaftliche Verlag Als Mittler 175 Jahre B.G. Teubner 1811–1986, Vieweg +Teubner Verlag, Wiesbaden, 1986, 27–72.

[51] A. Reuss, Berechnung der Fließgrenze von Mischkristallen auf Grund der Plastizitätsbedingung für Einkristalle., ZAMM, J. Appl. Math. Mech./ Zeitschrift Für Angewandte Mathematik Und Mechanik 9 (1929) 49–58.

[52] R. Hill, The elastic behaviour of a crystalline aggregate, Proc. Phys. Soc. Section A 65 (1952).

[53] K.B. Panda, K.S.R. Chandran, First principles determination of elastic constants and chemical bonding of titanium boride (TiB) on the basis of density functional theory, Acta Mater. 54 (2006) 1641–1657.

[54] J. Navarro-Sánchez, I. Mullor-Ruíz, C. Popescu, D. Santamaría-Pérez, A. Segura, D. Errandonea, J. González-Platas, C. Martí-Gastaldo, Peptide metal-organic frameworks under pressure: flexible linkers for cooperative compression, Dalton Trans. 47 (2018) 10654–10659.

[55] S.F. Pugh, XCII. Relations between the elastic moduli and the plastic properties of polycrystalline pure metals, Lond. Edinb. Dublin Philos. Mag. J. Sci. 45 (1954) 823–843.

[56] I.N. Frantsevich, Elastic constants and elastic moduli of metals and insulators, Reference Book (1982).

[57] K. Shirai, A study of negative force constants: a method to obtain force constants by electronic structures, J. Solid State Chem. 133 (1997) 327–334.

[58] N. Guechi, A. Bouhemadou, R. Khenata, S. Bin-Omran, M. Chegaar, Y. Al-Douri, A. Bourzami, Structural, elastic, electronic and optical properties of the newly synthesized monoclinic Zintl phase BaIn$_2$P$_2$, Solid State Sci. 29 (2014) 12–23.

[59] M.I. Kholil, M.T.H. Bhuiyan, Physical properties of spinel-type superconductors CuRh$_2$S$_4$ and CuRh$_2$Se$_4$: A DFT study, Results Phys. 12 (2019) 73–82.

[60] H. Chen, L. Yang, Pressure effect on the structural and elastic property of Hf$_2$InC, Phys. B Condens. Matter 406 (2011) 4489–4493.

[61] M.E. Fine, L.D. Brown, H.L. Marcus, Elastic constants versus melting temperature in metals, Scr. Metall. 18 (1984) 951–956.

[62] V.N. Belomestnykh, E.P. Tesleva, Interrelation between anharmonicity and lateral strain in quasi-isotropic polycrystalline solids, Tech. Phys. 49 (2004).

[63] A.L.J. Pereira, O. Gomis, J.A. Sans, J. Contreras-García, F.J. Manjón, P. Rodríguez-Hernández, A. Muñoz, A. Beltrán, β-Bi$_2$O$_3$ under compression: optical and elastic properties and electron density topology analysis, Phys. Rev. B 93 (2016) 224111.

[64] A.L.J. Pereira, D. Errandonea, A. Beltrán, L. Gracia, O. Gomis, J.A. Sans, B. García-Domene, A. Miquel-Veyrat, F.J. Manjón, A. Muñoz, C. Popescu, Structural study of α-Bi$_2$O$_3$ under pressure, J. Phys. Condens. Matter 25 (2013) 475402.

[65] N. Choudhury, S.L. Chaplot, Ab initio studies of phonon softening and high-pressure phase transitions of α-quartz SiO$_2$, Phys. Rev. B 73 (2006) 094304.

[66] D. Errandonea, M. Somayazulu, D. Häusermann, Phase transitions and amorphization of CaWO$_4$ at high pressure, Phys. Status Solidi (B) Basic Res. 235 (2003) 162–169.

[67] G. Serghiou, H. Reichmann, Size criterion for amorphization of molecular ionic solids, Phys. Rev. B 55 (1997) 14765.

[68] M.G. Vergniory, L. Elcoro, Z. Wang, J. Cano, C. Felser, M.I. Aroyo, B.A. Bernevig, B. Bradlyn, Publisher's note: graph theory data for topological quantum chemistry, Phys. Rev. E 96 (2017) 023310.

[69] L. Wu, F. Tang, X. Wan, Exhaustive list of topological hourglass band crossings in 230 space groups, Phys. Rev. B 102 (2020) 035106.